OPEN

Observing Optical Plasmons on a Single Nanometer Scale

Moshik Cohen[1,2], Reuven Shavit[2] & Zeev Zalevsky[1,3]

[1]Faculty of Engineering, Bar-Ilan University, Ramat-Gan 52900, Israel, [2]Department of Electrical and Computer Engineering, Ben-Gurion University of the Negev, Beer-Sheva 84105, Israel, [3]Bar-Ilan Institute for Nanotechnology & Advanced Materials, Ramat-Gan 52900, Israel.

The exceptional capability of plasmonic structures to confine light into deep subwavelength volumes has fashioned rapid expansion of interest from both fundamental and applicative perspectives. Surface plasmon nanophotonics enables to investigate light - matter interaction in deep nanoscale and harness electromagnetic and quantum properties of materials, thus opening pathways for tremendous potential applications. However, imaging optical plasmonic waves on a single nanometer scale is yet a substantial challenge mainly due to size and energy considerations. Here, for the first time, we use Kelvin Probe Force Microscopy (KPFM) under optical illumination to image and characterize plasmonic modes. We experimentally demonstrate unprecedented spatial resolution and measurement sensitivity both on the order of a single nanometer. By comparing experimentally obtained images with theoretical calculation results, we show that KPFM maps may provide valuable information on the phase of the optical near field. Additionally, we propose a theoretical model for the relation between surface plasmons and the material workfunction measured by KPFM. Our findings provide the path for using KPFM for high resolution measurements of optical plasmons, prompting the scientific frontier towards quantum plasmonic imaging on submolecular scales.

S urface Plasmon Polaritons (SPPs) are optically excited collective charge oscillations, which can propagate along metal - dielectric interface[1]. These electromagnetic waves are characterized by subdiffraction volumes and high intensities, properties which unlock the potential for huge variety of applications[2-6]. Nevertheless, since being bound to the surface and confined to deep subwavelength scales, high resolution imaging of nano-plasmonic modes using conventional optical microscopy is nearly impossible[7-9]. Subdiffraction optical imaging of surface plasmons can be achieved using near field techniques, as scanning near field optical microscope (SNOM) and its modifications that use metal tips[10-15]. In SNOM, a subwavelength optical aperture samples the average optical signal intensity as a function of position. However, spatial resolution and collection efficiency are both limited by the aperture size and by the distance between a sample and the tip. This is mainly because SNOM samples only the decaying or evanescent part of the optical signal outside the nanoscale object[16]. To date smallest commercially available SNOM tips achieve aperture diameters of 50 nm - 100 nm (Nanonics - Optometronic 4000™ at http://www.nanonics.co.il/products/nsom-spm-systems/optometronic-4000.html). Phase resolved imaging of optical near field with resolution on the order of 10 nm – 20 nm was recently demonstrated using Heterodyne and pseudoheterodyne scattering type SNOM[17] (s-SNOM). Plasmonic imaging with nanometric spatial resolution can also be achieved using electron energy loss spectroscopy (EELS)[18–20], with time resolved measurements are also demonstrated using laser excited photo cathodes in electric microscopy[21,22]. Kelvin probe force microscopy (KPFM), also known as surface potential microscopy, is a variant of atomic force microscopy (AFM) which was first introduced in 1991[23]. KPFM enables to measure the work function difference between a scanning tip and a surface with submolecular resolution and submilivolt sensitivity[24–28]. When a scanning probe tip is electrically connected to a conductive sample, a contact potential difference (CPD) will arise due to the different workfunctions of the tip and the sample. KPFM measures local variations in the CPD by applying a voltage between the sample and the tapping AFM tip so that the electric field caused by the CPD and the resulting force on the tip are compensated. For a certain tip position, the compensating voltage represents the local contact potential difference (LCPD) and can be determined either with a feedback loop or by measuring the voltage dependence frequency shift[23,26,29–31]. Recently, we used KPFM and space-time Fourier analysis to characterize a nanoplasmonic device with resolution of 10 nm[32]. However, no imaging mechanism of SPPs with KPFM has so far been presented, and achieving single nanometer resolution imaging of optical fields is an extraordinary practice. Here, we show that KPFM can image and characterize surface plasmon polaritons with resolution at

the single nanometer scale. A theoretical model is proposed to define the relation between CPD and SPPs and provide an in-depth understanding of the imaging mechanism. We characterize plasmonic nanoantenna and waveguiding structures achieving measurement sensitivity of only 2 nm. Additionally, we observe that the sign of the CPD can be used to obtain information on the electric field's directionality, towards full vector characterization of SPPs. Figure 1 illustrates the process of SPP characterization with scanning KPFM. The origin of nanoplasmonic sensing with KPFM lies in the fact that KPFM measures the contact potential difference (CPD) between the scanning probe tip and the surface[26,33]. The CPD is closely related with the charge distribution on the surface, as well as with the surface plasmon polaritons[34–40]. When nanometallic structures are illuminated with optical radiation, coherent oscillations of free electrons are excited on the surface. These highly confined optically induced charge density waves preserve the frequency of incident photons and strongly affect the work function in the vicinity of the device. Optically excited variations in the workfuction of CdSe nanowires[41] and 2D array of subwavelength apertures[42] was recently characterized by EFM and KPFM.

Results

According to the Lorentz model, the motion of electrons in metals is governed by a second order partial differential equation

$$m\left[\frac{\partial^2 x}{\partial t^2} + \Gamma \frac{\partial x}{\partial t} + \Omega^2 x\right] = -eE \qquad (1)$$

Here m and e is the electron mass and charge, respectively; x is the electron displacement from the nucleus $\Gamma = \frac{1}{\tau}$ is the damping rate, Ω is the spring constant and E is the electric field. Assuming time harmonic behavior for the electric field and displacement, neglecting Ω in the free electron region yields the Drude polarizability:

$$P = -Nex = -\frac{Ne^2}{m}\frac{1}{\omega^2 + i\Gamma\omega}E(x,t) \qquad (2)$$

where $\omega = 2\pi f$ is the optical angular frequency of the electric field. The in plane relative permittivity ($\varepsilon_\parallel \equiv \varepsilon_r + i\varepsilon_i$) can be extracted from Equation 2, using $\varepsilon = 1 + P/E$. The real and imaginary part of $\varepsilon_\parallel$ are attributed intraband and interband transitions, respectively. Extended Drude model which considers the restoration force (Ω) is a preferred analytical description at the bound electron region. This model achieves excellent agreement for Au within 500 nm–1000 nm wavelength range[43]. Further improvement to the extended Drude model can be obtained by adding terms which carefully

describe the critical points (CP)[44,45]. Near the plasma frequency, $\omega \approx \omega_p = \sqrt{Ne^2/m\varepsilon_0}$, the relative permittivity is very small ($\varepsilon(\omega_p) \to 0$). Hence, $E(x, t)$ becomes a pure depolarization field with quanta of these charge oscillations are referred to as plasmons. Using the relation between polarization and charge density $\rho_{pol} = -\nabla \cdot P$, the surface electric potential is calculated by integrating the charge density function over the computational surface

$$V(r) = \iint \frac{\rho_{pol}(r)}{4\pi\varepsilon_0 |r - r'|} \, ds' \qquad (3)$$

The charge density function may also be obtained by solving the Fock equations using an exchange potential operator[46,47], a more accurate solution but computationally expensive when obtained numerically. The experimental setup used in this work is depicted in Figure 2a. The sample is illuminated from above by unfocused He-Ne laser at wavelength of 633 nm ($\omega = 2.98 \cdot 10^{15} r/s$) at incident angle of 45°. The light beam is linearly polarized in parallel with the dipole orientation, with the sample is appropriately oriented to avoid the cantilever from blocking the light path to the devices. Since $\omega \gg \Gamma \sim 10^{13}$, the in plane relative permittivity can be written as $\varepsilon_\parallel = \varepsilon_B - \omega_p^2/\omega^2 + i\omega_p^3/\omega^2\tau$, with ε_B is the contribution of bound electrons and ω_p is the plasma frequency. In our measurements topography and KFPM images are recorded sequentially using the lift mode technique to minimize cross talk between the measurements[48]. To this end, we first acquire the surface topography of a single line in tapping mode and then retrace this topography over the same line at a set lift height from the surface to measure the KPFM signal. To map the workfunction of the sample, we apply both AC voltage (V_{AC}) and a DC voltage (V_{DC}) to the AFM tip. V_{AC} generates oscillating electrical forces between the AFM tip and sample surface, and V_{DC} nullifies the oscillating electrical forces that originated from CPD between tip and sample surface. In our study, the tip - sample distance (H) significantly influence the resolution and sensitivity of the measurements. For small values of H, the KPFM image is dominated by short range forces ($\sim H^{-6}$) like Van der Waals and capillary interactions. However, for larger values of H, long range electrostatic and magnetic interactions ($\sim H^{-2}$) govern the results. Therefore, it is critical to optimize the lift height for high quality imaging. To demonstrate unambiguously that we can measure and image plasmonic waves with nanoscopic resolution and sensitivity we chose to investigate hybrid devices of dipole nanoantennas integrated with metal - insulator - metal (MIM) plasmonic waveguides as shown in Figure 2b. These devices are of prime importance for large variety
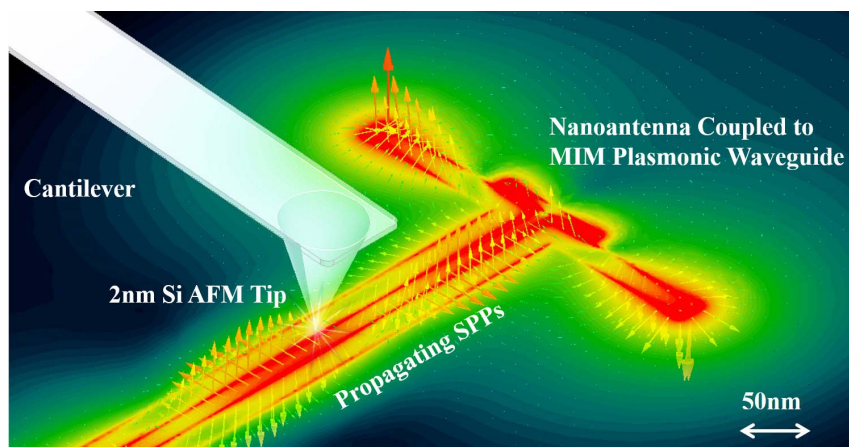

Figure 1 | Illustration of nanoplasmonic characterization with KPFM. Dipole nanoantenna is connected to MIM waveguide with nanometric gap width. The device is illuminated by a laser and the excited plasmons change the CPD between the tip and the surface, which measured by KPFM with nanometric resolution.
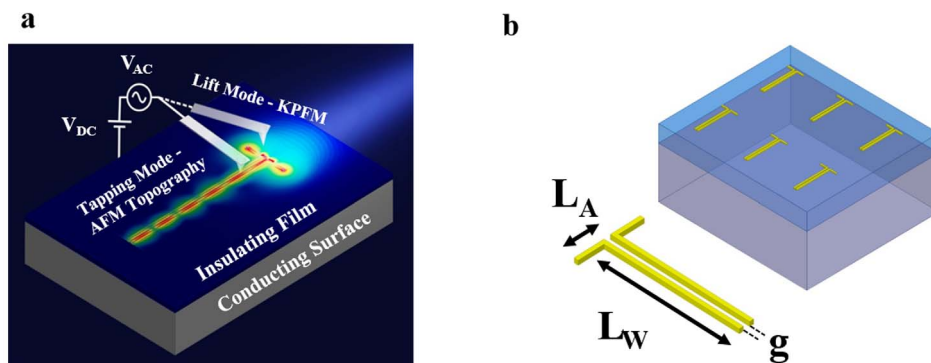
Figure 2 | Schematics description of our KPFM experimental process and fabricated devices. (a), Schematic of the measurement principle. First the topography is acquired in tapping mode, then the tip elevates to a set lift height, H to create the CPD map. (b), Description of the analyzed nanoplasmonic devices. Dipole nanoantenna with arm length 'L$_A$' and gap 'g', are connected to MIM waveguide of length L$_W$. The thickness and width of all metal strips are 12 nm.

of applications[49,50], and have several advantages for this study. First, the combination of nanoantenna and plasmonic waveguide enables to image both localized and propagating SPPs. Localized SPPs are optically excited at the nanoantenna and are coupled to propagating modes along the waveguide. Furthermore, by comparing CPD images with calculated vector fields we show that KPFM measurements may provide information on the vector optical near field. The devices where fabricated by electron beam lithography (EBL), ion beam sputtering (Ag, 10 nm) and lift off. By fabricating the structures on the insulating layer of a Si substrate (2 μm thick SiO$_2$), we avoid coupling effects between the conducting Si and the metallic device. After the lift off the PMMA is completely removed, allowing contact between the AFM tip and the metallic devices. Figure 3a presents a scanning electron microscopy (SEM) image of the

analyzed device, with geometrical dimensions of L$_W$ = 750 nm, L$_A$ = 100 nm, and g = 12 nm. The image was recorded at beam current of 0.4 nA and low accelerating voltage of 5 kV. Figure 3b shows an AFM topography image of the device in 3D, obtained using Si tip with 2 nm typical diameter. Subsequently, KPFM characterization of the same device was performed in lift mode while the device is illuminated by a He-Ne Laser. The KPFM measurements were performed for tip - sample distances ranging from 10 nm–250 nm, with the stage remains spatially fixed and the tip is scanned. We observe that for small values of H, short range interactions strongly affect the KPFM image. For larger tip-sample distances, the results are governed by the long range interactions. The range of distances for which we obtained the best resolution was between 30 nm–50 nm. Figure 3c shows the KPFM image recorded for tip-sample distance of
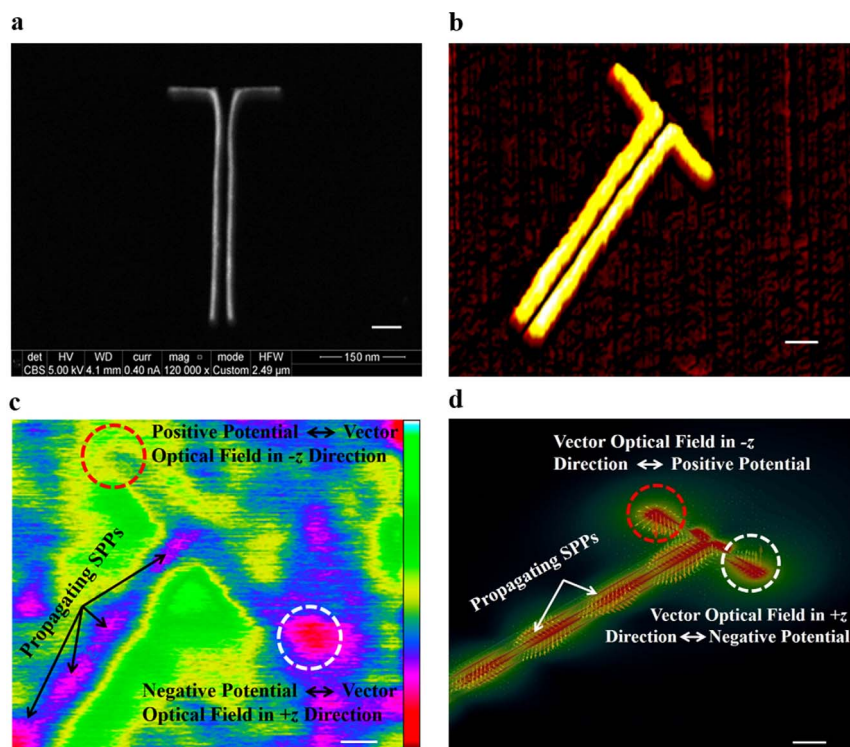

Figure 3 | SEM, AFM KPFM and numerical analysis of MIM nanoplasmonic device. (a), High resolution SEM image of the fabricated and analyzed device (b), 3D AFM topography image of the device. The image was recorded with Si super sharp tip with 2 nm aperture. (c), CPD image of the device under optical illumination with He-Ne laser at frequency of 474 THz, recorded with the same tip as (b). KPFM Signal scale bar: −1.7 V–+1.7 V. (d), 3D Numerical calculation (FEM) results of the of the analyzed device under optical illumination of He-Ne laser, similar to the experimental setup used to obtain the results in (c). Scale bar: 50 nm.
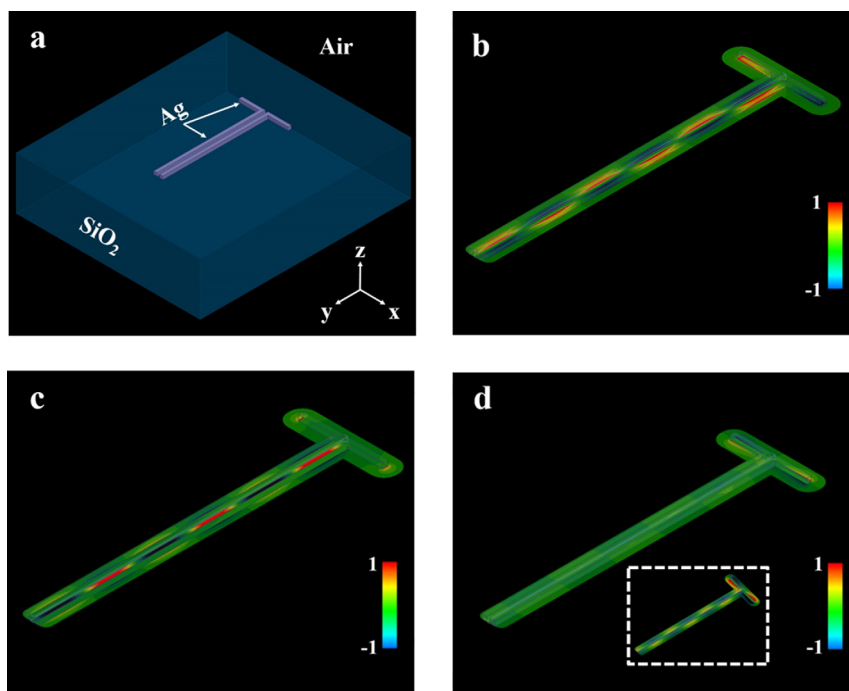
Figure 4 | Energy transport and propagation properties of dipole nanoantenna coupled to MIM nanoplamonic waveguide. (a), 3D Schematics of the analyzed devices (b), Numerically calculated near-field image showing $Re(E_z) = |E_z|cos(\phi_z)$. (c), Numerically calculated near-field image showing $Re(E_x) = |E_x|cos(\phi_x)$. (d), Numerically calculated near-field image showing $Re(E_y) = |E_y|cos(\phi_y)$, with the inset shows E_y for normalized field scale of $\pm 1/4$ (instead of ± 1).

$H = 35$ nm, which exhibits clear nanometric resolution. We observe two dipolar-like modes on the antenna segments, with strong fields at the antenna ends and at the gap, as expected for a dipole plasmonic nanoantenna in the visible[32]. The localized fields at the nanoantenna gap extend along the MIM waveguide, periodically changing their polarity. The modal behavior of the propagating SPPs along the waveguide is observed in the KPFM image (Fig. 3c). Four periods of modes appear along the waveguide, represented by peaks of the KPFM signal, as the measured[32] SPP wavelength is 240 nm. The shape of the waveguide, as well as the field decay into its metallic arms are very well captured. This provides direct experimental imaging of a propagating surface plasmon polaritons, obtained for the first time for channel waveguides with 12 nm×10 nm gap cross-ection. Strong localized fields are observed also on the exterior metal - insulator interfaces of the waveguides, as predicted by the theory of SPPs[1]. We observe that the measured KPFM fields on the ends of the nanoantenna are inversely polarized, with the field on the left edge is positive +1.5 V and the field on the right edge is negative −1.5 V, corresponds to local optical near field direction of $+\hat{z}$ and $-\hat{z}$, respectively (see Fig. 3d). This behavior is reproduced in numerical calculation results, presented at the optical frequency of 474 THz (633 nm). The numerical results are obtained using Ansys High Frequency Structure Simulator (HFSS V15[32,51,52]) based on the finite element method (FEM). Generally, the electric field is described by a three dimensional vector $\mathbf{E} = (E_x, E_y, E_z)$, where each field component E_i is characterized by both magnitude $|E_i|$ and a phase ϕ_i[53]. Figure 3d presents the 3D electric field vector, $|\mathbf{E}|$, with each arrow represents the direction of the local electric field vector. In spherical coordinates system, the angles θ, φ of each arrow shown in Figure 3d are the angles define the direction of the local near field vector. Figure 4 shows the numerically calculated scalar components of the electric fields on the device. Figure 4b shows the real part of the vertical near-field component $Re(E_z) = |E_z|cos(\phi_z)$ where $|E_z|$ is the near-field amplitude and ϕ_z the phase. We observe high intensity at the nanoantenna ends and gap as well as periodical change in the field polarity, as expected for optical gap nanoantennas[17]. For the horizontal near field component E_x, as shown in Figure 4c. For $Re(E_x)$, we can see that the amplitude image exhibits a completely different pattern, featuring a highly localized, intense fields at the nanoantenna gap and ends with a spatially constant phase[17]. Similarly, for the E_x near field component, there is no phase difference between the two waveguide arms. Since E_x has significantly higher amplitude than E_z, the phase behavior inside the waveguide is dominated by E_x. This result explains why no phase difference between the fields inside the waveguide is observed in the KPFM image (Fig. 3c). As expected, the E_y component of the near field exhibits much lower enhancement, see Figure 4d. Interestingly, the phase structure of E_y may explain the slight shift of the phase center of the KPFM signal (Fig. 3c) with respect to the topography. Figure 5a presents a high resolution AFM image of the fabricated device with gap of 4 nm ($g = 4$ nm, $L_A = 20$ nm), which sets the lower limit for the gap width achievable via our EBL fabrication process. The KPFM signal of the corresponding topography is shown in Figure 5b. The device exhibits lower field enhancement, which may be attributed to the off resonance dimensions. Additionally, the gap width may approach ~1 nm at some points due to undesired roughness of the lithography process. This may lead to decreased field enhancement originated from quantum charge transfer[54]. Figure 5c shows the topography (blue) and KPFM (black) of the device plotted along the dipole axis. We observe that the KPFM signal of the different nanoantenna arms can be clearly resolved, while separated by only ~4 nm gap. This provides first direct experimental evidence of KPFM capability to image surface plasmon modes with unprecedented resolution on the order of a single nanometer. This imaging resolution of KPFM holds potential for further improvements which can be obtained using sharper tips and process optimization[24] Now, we demonstrate another substantial vantage of KPFM for plasmonic characterization, by resolving the propagation properties of MIM waveguides with gap (g) difference of 2 nm. Figure 6a presents the configuration of the analyzed devices. Figure 6b shows the calculated electric field at frequency of 474 THz ($\lambda = 633$ nm,) for devices with $L_W = 900$ nm, $g = 10$ nm, 20 nm, 30 nm and 60 nm. We observe
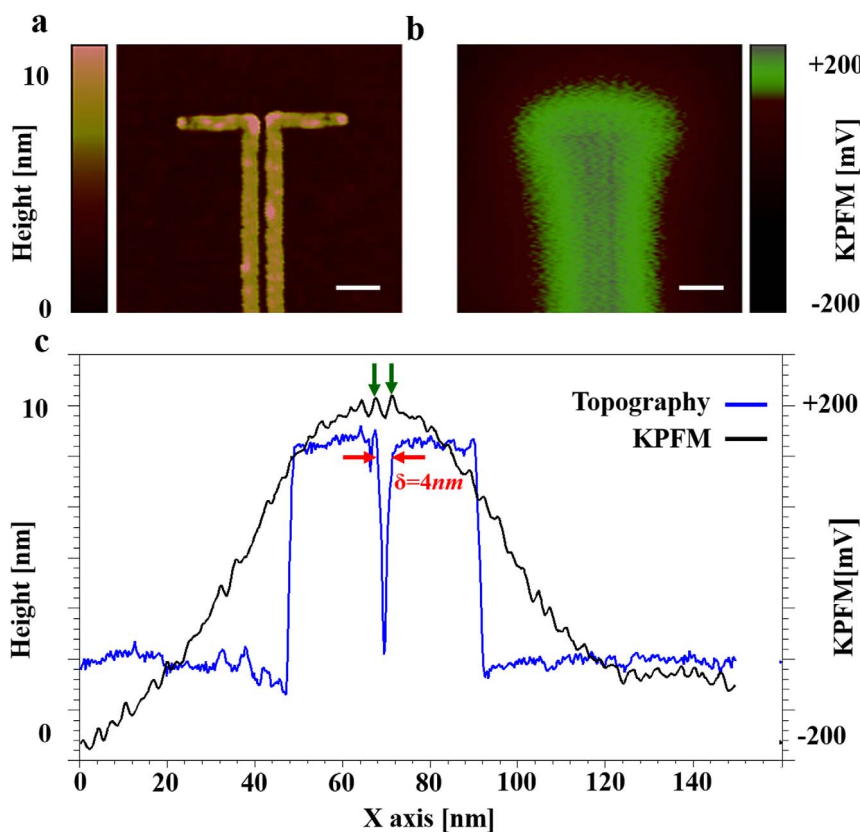
Figure 5 | Experimental demonstration of KPFM resolution in plasmonic imaging. (a), High resolution AFM image of the device with g = 4 nm, L_A = 20 nm (b), Corresponding KPFM map of the same device under optical illumination (c), Experimental topography (blue line) and KPFM (black line) across the nanoantenna axis. Scale bar: 20 nm.

inverse relation between the wavelength of the propagating SPPs, λ_{SPP}, and the gap width. As the gap width decreases, the plasmons are confined in both dimensions and vice versa; a confinement which increases the propagation loss. This nonlinear dispersion behavior is evidenced by the difference number of SPP periods propagate within the waveguide. For g = 10 nm, seven periods of SPP modes are contained inside the waveguide, as for g = 60 nm only four periods are observed (see Fig 6b). The calculated electric field along the center of the waveguide (dashed line in Fig. 6a) is shown in Figure 6c, which further demonstrate the change in λ_{SPP} as the gap width increases. Figure 6d shows the KPFM signal map for g = 30 nm and tip - sample distance of H = 35 nm, selected for maximum resolution. This image has similar characteristics to Figure 3c with two main differences. First, only three periods of SPPs are contained within the waveguide (compared with four periods in Fig. 3c), this is due to the increase in gap width from 12 nm to 30 nm; a result which is in very good agreement with our calculations (Fig 6b). Second, lower field intensities are observed at the gap and on both nanoantenna ends, mainly caused by impedance mismatch between the dipole and the waveguide and by geometrical shift from resonance. The exact spatial frequency of the propagating SPPs is detected by analyzing the frequency content of the KPFM measurements along the waveguide via spatial Fourier transform (FFT). The black graph in Figure 6e presents the results of spatial FFT performed on the KPFM signal inside the waveguide (marked by line 1 in Fig. 6d), with the blue curve corresponds to spatial FFT performed outside the device (line 2). Both measurements shown in Figure 6e have dominant field component at low frequencies, a result which is in good agreement with the general electrostatic character of KPFM and can be referred to the standing waves in the structure. However, we observe strong spatial frequency component in the field along the device, λ_{SPP} = 248 nm. The amplitude of this component is 15dB higher than the

corresponding component in the measurement described by the blue curve, providing solid evidence for the existence of propagating SPPs inside the waveguide. We used this method to characterize the propagation properties is a series of fabricated nanoplasmonic devices with gap width varying between 10 nm–30 nm in steps of only 2 nm (i.e. g = 10 nm, 12 nm,…30 nm), L_A = 100 nm and L_W = 3000 nm. For each KPFM measurement, we found λ_{SPP} by performing spatial FFT and measuring the plasmon - wavelength at the peak of the curve (see Fig. 6e).We use long waveguides ($L_W \gg \lambda_{SPP}$) in order to minimize the standing waves in the device and improve the sensitivity. Figure 7a shows the experimentally obtained dispersion curve (blue graph), with the calculation results presented in the black curve. Real time image of the characterization process via KPFM under laser illumination if presented in Figure 7b. We observe different experimentally obtained plasmon propagation wavelength (λ_{SPP}) for waveguides with gap difference of 2 nm, which confirm that KPFM can resolve SPPs with 2 nm resolution, currently limited by the aperture dimensions of the scanning probe. The maximum deviation between the calculated and experimental dispersion curves is δ = 2.5 nm, less than 1% from the mean λ_{SPP}.

Discussion
In Summary, we introduced KPFM as an exceptional method for imaging and characterization of plasmonic modes at optical frequencies. By investigating channel waveguides coupled to nanoantennas, we characterized both surface plasmons and surface plasmon polaritons at the nanoscale. We characterized a variety of nanoplasmonic devices, with experimentally demonstrated spatial resolution and sensitivity both on the order of a single nanometer. The KPFM images include information on the amplitude and phase of the optical near field, and are of good agreement with full wave numerical
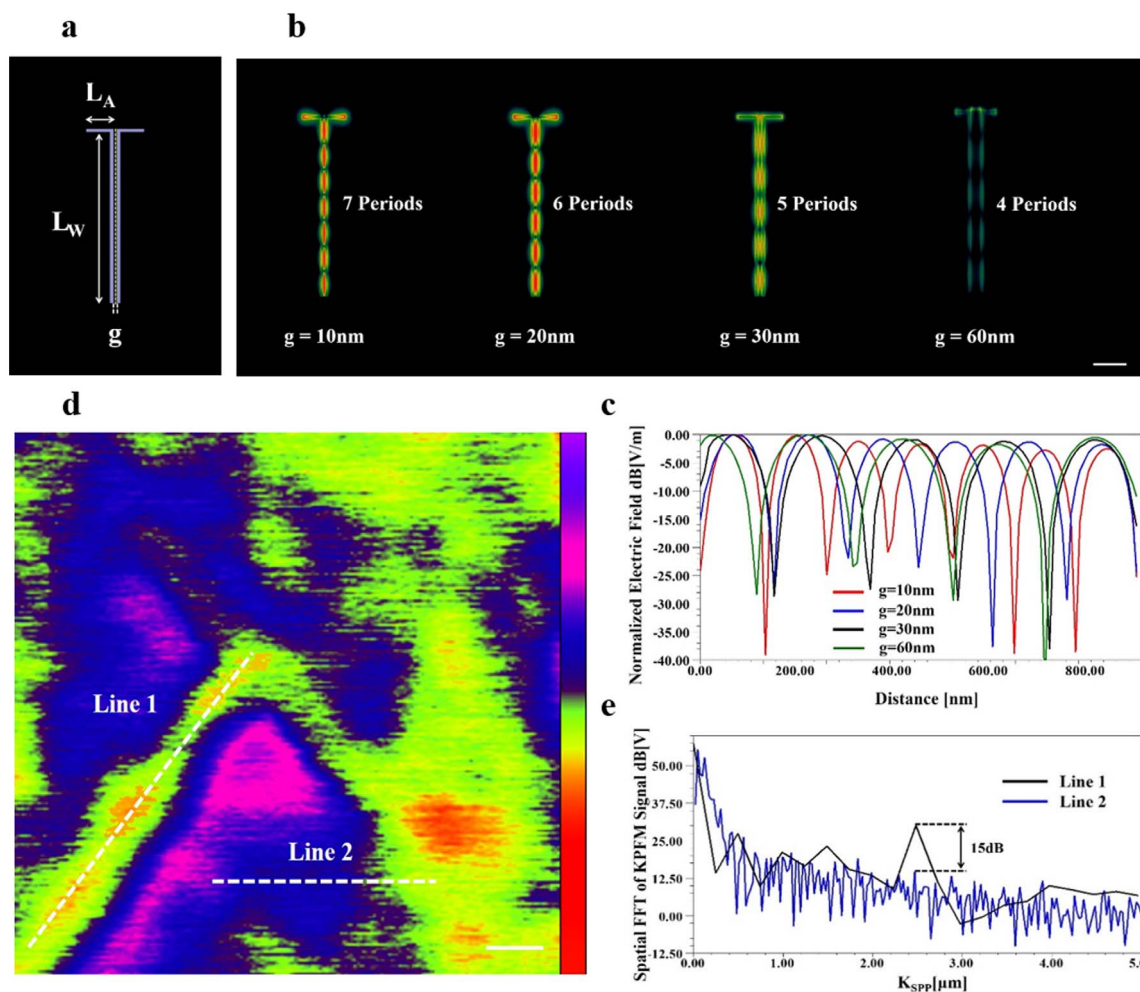
Figure 6 | Spatial frequency analysis of the nanoplasmonic devices using KPFM, spatial FFT and numerical calculations. (a), Device configuration. (b), Numerically calculated magnitude of the optical near field, |E| devices with g = 10 nm, 20 nm, 30 nm and 60 nm, under optical illumination. Decrease in the spatial frequency (higher λ_{SPP}) is observed when g is increased. (c), Calculated |E| at 474 THz, plotted along the center of the MIM waveguides (dashed line in a) (d), CPD image of the device under optical illumination recorded at H = 35 nm. KPFM Signal scale bar: ±1.2 V (e), Spatial FFT results of the KPFM signal inside (black graph, calculated along Line 1 in (d)) and outside the waveguide (Line 2 in (d)). Scale bars: 100 nm in (a) and 50 nm in (d).
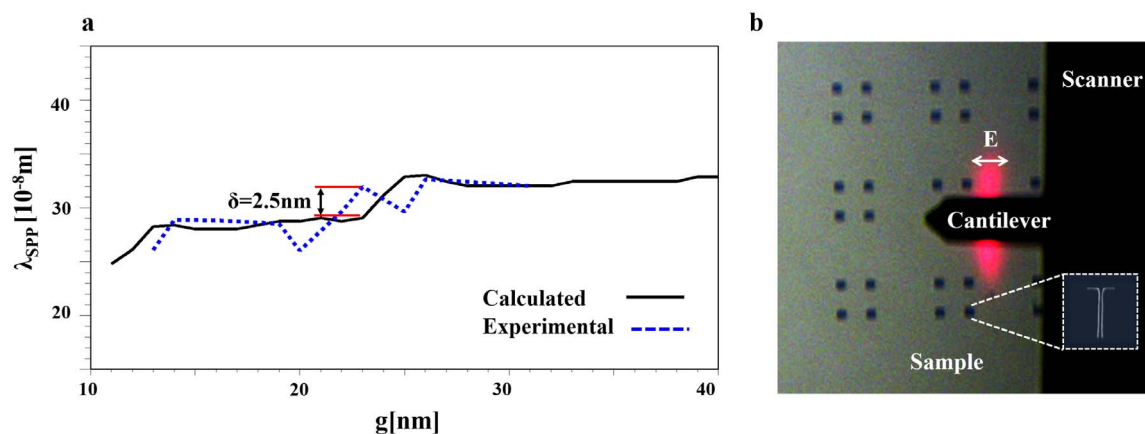

Figure 7 | SPP Characterization with 2 nm resolution. (a), λ_{SPP} as a function of the gap width, g, obtained experimentally (blue dots) and theoretically (continuous black curve). (b), Real time image of the characterization process, captured from the AFM system. Each square includes nanoantennas and MIM waveguide with different gap width. The laser polarization is aligned with the dipole orientation.

calculations. Our findings open the way for using KPFM under optical illumination for direct imaging of SPPs with nanometric spatial resolution and sensitivity, establishing KPFM as a preferred candidate for experimental characterization of SPP nano devices. It will now be possible for broad community of KPFM users to investigate optically induced charge density waves with dimensions compatible to state of the art future CMOS technology nodes.

Methods

AFM and KPFM measurements. All measurements were performed at room temperature and free ambient conditions (no vacuum), using Dimension Icon AFM system with NanoScope V controller (Bruker®). For both AFM and KPFM measurements, we used NanoWorld probes SSS-NCH, SuperSharpSilicon - Non-Contact/Tapping™ mode - High resonance frequency; with typical diameter of 2 nm, resonance frequency of 320 kHz and spring constant of 42 N/m. typically, voltages of 2 V, ac capacitance frequencies of 880 MHz, lift heights of 30 nm–50 nm and line rates of 0.1 KHz were employed.

Numerical simulations. The numerical results are obtained by using the software package ANSYS HFSS™ V15, the industry-standard simulation tool for 3D full-wave electromagnetic field simulation. HFSS solve Maxwell's equations via the finite element method (FEM) using adaptive mesh refinement process for tailored accuracy requirements. The field's solutions are calculated with the metallic (Ag) plasmonic structures being deposited on a homogenous SiO2 substrate. The nanoantenna is illuminated by optical sources at 474 THz (wavelength of 633 nm), which are modeled as focused Gaussian beams with 1 μm characteristic diameter. The electric field is polarized in parallel with the dipole direction, as the wave vector **K** is perpendicular. A selectively dense meshing is assigned in the metallic and waveguiding regions, with maximum cell size of 1 nm and 750,000 FEM tetrahedral cells. To provide maximum accuracy, the model is terminated as following: the interface with free space is bounded by perfectly matched layer (PML) absorbing boundary conditions (ABC), while the metallic and SiO2 termination are done via layered impedance (LI) ABC. The minimum number of adaptive meshing iterations was set to 12, with convergence condition of 1% maximum energy variance between adjacent iterations.

Devices Fabrication. SiO2/Si sample was spin-coated with poly (methyl methacrylate) (PMMA 950 A2) electron-beam resist providing thickness of 100 nm. The samples coated with PMMA were subsequently baked for 120 s on a hotplate at 180C. The desired pattern was exposed in the PMMA layer using a CRESTEC CABLE-9000C high-resolution electron-beam lithography system using different doses to control line and gap width. Then the samples were developed for 90 sec using methyl isobutyl ketone (MIBK), and rinsed with IPA. The samples were subsequently exposed to Ar plasma to etch 10 nm in order to remove leftovers from the pattern, sputtered using BESTEC 2″ DC magnetron to deposit 3 nm Cr, and 13 nm Au, then immersed in 180 Khz ultrasonic bath with NMP for 3 h for resist liftoff.

1. Maier, S. A. *Plasmonics: Fundamentals and Application.* (Springer, 2007).
2. Schuller, J. A. *et al.* Plasmonics for extreme light concentration and manipulation. *Nat. Mater.* **9**, 193–204 (2010).
3. Gramotnev, D. K. & Bozhevolnyi, S. I. Plasmonics beyond the diffraction limit. *Nat. Photonics* **4**, 83–91 (2010).
4. Atwater, H. A. & Polman, A. Plasmonics for improved photovoltaic devices. *Nat. Mater.* **9**, 205–213 (2010).
5. Berini, P. & Leon, I. D. Surface plasmon-polariton amplifiers and lasers. *Nat. Photonics* **6**, 16–24 (2012).
6. Graydon, O. Sensing: Plasmonic interferometry. *Nat. Photonics* **6**, 139–139 (2012).
7. Abbe, E. Beiträge zur Theorie des Mikroskops und der mikroskopischen Wahrnehmung. *Arch. Für Mikrosk. Anat.* **9**, 413–418 (1873).
8. Sommerfeld, A. Ueber die Fortpflanzung elektrodynamischer Wellen längs eines Drahtes. *Ann. Phys.* **303**, 233–290 (1899).
9. Heisenberg, W. Über den anschaulichen Inhalt der quantentheoretischen Kinematik und Mechanik. *Z. Für Phys.* **43**, 172–198 (1927).
10. Schnell, M. *et al.* Nanofocusing of mid-infrared energy with tapered transmission lines. *Nat. Photonics* **5**, 283–287 (2011).
11. Inouye, Y. & Kawata, S. Near-field scanning optical microscope with a metallic probe tip. *Opt. Lett.* **19**, 159–161 (1994).
12. Betzig, E., Lewis, A., Harootunian, A., Isaacson, M. & Kratschmer, E. Near Field Scanning Optical Microscopy (NSOM). *Biophys. J.* **49**, 269–279 (1986).
13. Hillenbrand, R., Taubner, T. & Keilmann, F. Phonon-enhanced light–matter interaction at the nanometre scale. *Nature* **418**, 159–162 (2002).
14. Esteban, R. *et al.* Direct Near-Field Optical Imaging of Higher Order Plasmonic Resonances. *Nano Lett.* **8**, 3155–3159 (2008).
15. Fei, Z. *et al.* Gate-tuning of graphene plasmons revealed by infrared nano-imaging. *Nature* **487**, 82–85 (2012).
16. Batson, P. E. Plasmonic Modes Revealed. *Science* **335**, 47–48 (2012).
17. Duan, H., Fernández-Domínguez, A. I., Bosman, M., Maier, S. A. & Yang, J. K. W. Nanoplasmonics: Classical down to the Nanometer Scale. *Nano Lett.* **12**, 1683–1689 (2012).
18. Scholl, J. A., García-Etxarri, A., Koh, A. L. & Dionne, J. A. Observation of Quantum Tunneling between Two Plasmonic Nanoparticles. *Nano Lett.* **13**, 564–569 (2013).
19. Iberi, V., Mirsaleh-Kohan, N. & Camden, J. P. Understanding Plasmonic Properties in Metallic Nanostructures by Correlating Photonic and Electronic Excitations. *J. Phys. Chem. Lett.* **4**, 1070–1078 (2013).
20. Zewail, A. H. Four-Dimensional Electron Microscopy. *Science* **328**, 187–193 (2010).
21. Kim, J. S. *et al.* Imaging of Transient Structures Using Nanosecond in Situ TEM. *Science* **321**, 1472–1475 (2008).
22. Nonnenmacher, M., O'Boyle, M. P. & Wickramasinghe, H. K. Kelvin probe force microscopy. *Appl. Phys. Lett.* **58**, 2921–2923 (1991).
23. Mohn, F., Gross, L., Moll, N. & Meyer, G. Imaging the charge distribution within a single molecule. *Nat. Nanotechnol.* **7**, 227–231 (2012).
24. Grutter, P. Scanning probe microscopy: Seeing the charge within. *Nat. Nanotechnol.* **7**, 210–211 (2012).
25. Jacobs, H. O., Knapp, H. F. & Stemmer, A. Practical aspects of Kelvin probe force microscopy. *Rev. Sci. Instrum.* **70**, 1756 (1999).
26. Hoppe, H. *et al.* Kelvin Probe Force Microscopy Study on Conjugated Polymer/Fullerene Bulk Heterojunction Organic Solar Cells. *Nano Lett.* **5**, 269–274 (2005).
27. Spadafora, E. J., Demadrille, R., Ratier, B. & Grévin, B. Imaging the Carrier Photogeneration in Nanoscale Phase Segregated Organic Heterojunctions by Kelvin Probe Force Microscopy. *Nano Lett.* **10**, 3337–3342 (2010).
28. Burke, S. A. *et al.* Determination of the local contact potential difference of PTCDA on NaCl: a comparison of techniques. *Nanotechnology* **20**, 264012 (2009).
29. Sadewasser, S. *et al.* New Insights on Atomic-Resolution Frequency-Modulation Kelvin-Probe Force-Microscopy Imaging of Semiconductors. *Phys. Rev. Lett.* **103**, 266103 (2009).
30. Nony, L., Foster, A. S., Bocquet, F. & Loppacher, C. Understanding the atomic-scale contrast in Kelvin Probe Force Microscopy. *arXiv:0907.4015* (2009). doi:10.1103/PhysRevLett.103.036802.
31. Cohen, M., Zalevsky, Z. & Shavit, R. Towards Integrated Nanoplasmonic Logic Circuitry. *Nanoscale* (2013). doi:10.1039/C3NR00830D.
32. Melitz, W., Shen, J., Kummel, A. C. & Lee, S. Kelvin probe force microscopy and its application. *Surf. Sci. Rep.* **66**, 1–27 (2011).
33. Sommerhalter, C., Matthes, T. W., Glatzel, T., Jäger-Waldau, A. & Lux-Steiner, M. C. High-sensitivity quantitative Kelvin probe microscopy by noncontact ultra-high-vacuum atomic force microscopy. *Appl. Phys. Lett.* **75**, 286–288 (1999).
34. Barth, C. & Henry, C. R. Surface Double Layer on (001) Surfaces of Alkali Halide Crystals: A Scanning Force Microscopy Study. *Phys. Rev. Lett.* **98**, 136804 (2007).
35. Gross, L. *et al.* Measuring the Charge State of an Adatom with Noncontact Atomic Force Microscopy. *Science* **324**, 1428–1431 (2009).
36. König, T. *et al.* Measuring the Charge State of Point Defects on MgO/Ag(001). *J. Am. Chem. Soc.* **131**, 17544–17545 (2009).
37. Leoni, T. *et al.* Controlling the Charge State of a Single Redox Molecular Switch. *Phys. Rev. Lett.* **106**, 216103 (2011).
38. Bennett, A. J. Influence of the Electron Charge Distribution on Surface-Plasmon Dispersion. *Phys. Rev. B* **1**, 203–207 (1970).
39. Ekardt, W. Work function of small metal particles: Self-consistent spherical jellium-background model. *Phys. Rev. B* **29**, 1558–1564 (1984).
40. Schäfer, S., Wang, Z., Zierold, R., Kipp, T. & Mews, A. Laser-Induced Charge Separation in CdSe Nanowires. *Nano Lett.* **11**, 2672–2677 (2011).
41. Hutchison, J. A. *et al.* Tuning the Work-Function Via Strong Coupling. *Adv. Mater.* **25**, 2481–2485 (2013).
42. Vial, A., Grimault, A.-S., Macías, D., Barchiesi, D. & de la Chapelle, M. L. Improved analytical fit of gold dispersion: Application to the modeling of extinction spectra with a finite-difference time-domain method. *Phys. Rev. B* **71**, 085416 (2005).
43. Etchegoin, P. G., Le Ru, E. C. & Meyer, M. An analytic model for the optical properties of gold. *J. Chem. Phys.* **125**, 164705–164705–3 (2006).
44. Vial, A. & Laroche, T. Description of dispersion properties of metals by means of the critical points model and application to the study of resonant structures using the FDTD method. *J. Phys. Appl. Phys.* **40**, 7152 (2007).
45. Bardeen, J. Theory of the Work Function. II. The Surface Double Layer. *Phys. Rev.* **49**, 653–663 (1936).
46. Slater, J. C. & Krutter, H. M. The Thomas-Fermi Method for Metals. *Phys. Rev.* **47**, 559–568 (1935).
47. Jacobs, H. O., Knapp, H. F., Müller, S. & Stemmer, A. Surface potential mapping: A qualitative material contrast in SPM. *Ultramicroscopy* **69**, 39–49 (1997).
48. Dionne, J. A., Sweatlock, L. A., Atwater, H. A. & Polman, A. Plasmon slot waveguides: Towards chip-scale propagation with subwavelength-scale localization. *Phys. Rev. B* **73**, 035407 (2006).
49. Fu, Y. *et al.* All-Optical Logic Gates Based on Nanoscale Plasmonic Slot Waveguides. *Nano Lett.* **12**, 5784–5790 (2012).
50. Vicarelli, L. *et al.* Graphene field-effect transistors as room-temperature terahertz detectors. *Nat. Mater.* **11**, 865–871 (2012).

51. Murray, W. A., Suckling, J. R. & Barnes, W. L. Overlayers on Silver Nanotriangles: Field Confinement and Spectral Position of Localized Surface Plasmon Resonances. *Nano Lett.* **6**, 1772–1777 (2006).
52. Gersen, H., Novotny, L., Kuipers, L. & van Hulst, N. F. On the concept of imaging nanoscale vector fields. *Nat. Photonics* **1**, 242–242 (2007).
53. Schnell, M., Garcia-Etxarri, A., Alkorta, J., Aizpurua, J. & Hillenbrand, R. Phase-Resolved Mapping of the Near-Field Vector and Polarization State in Nanoscale Antenna Gaps. *Nano Lett.* **10**, 3524–3528 (2010).
54. Savage, K. J. *et al.* Revealing the quantum regime in tunnelling plasmonics. *Nature* **491**, 574–577 (2012).

Acknowledgments

Author contributions

M.C. initiated the project, carried out the theoretical design and analysis, designed the devices and the studies, performed the experiments, and wrote the manuscript. R.S. reviewed the manuscript and contributed the computing resources. Z.Z. contributed the experimental facility, reviewed the manuscript and participated in the analysis of the results.

Additional information

Competing financial interests: The authors declare no competing financial interests.

How to cite this article: Cohen, M., Shavit, R. & Zalevsky, Z. Observing Optical Plasmons on a Single Nanometer Scale. *Sci. Rep.* **4**, 4096; DOI:10.1038/srep04096 (2014).